processes

MDPI

Article

Dynamic Analysis of a Bolted Joint Rotor-Bearing System with a Blade–Casing Rubbing Fault

Chuanmei Wen [1], Zhimin Zhu [2], Xuezhong Fu [2,*], Tianliang Long [2] and Bing Li [2,3]

[1] School of Electronic Engineering, Guangxi University of Science and Technology, Liuzhou 545006, China; cmwen@gxust.edu.cn
[2] School of Mechanical and Automotive Engineering, Guangxi University of Science and Technology, Liuzhou 545006, China; 221068290@stdmail.gxust.edu.cn (Z.Z.)
[3] Guangxi Earthmoving Machinery Collaborative Innovation Center, Guangxi University of Science and Technology, Liuzhou 545006, China
* Correspondence: 100002350@gxust.edu.cn

Abstract: Bolted joints are widely used in aeroengine rotor systems to connect multiple components into an integrated structure and provide sufficient stiffness. The mechanical properties of a bolted joint have a significant effect on rotor dynamics. For modern aeroengine designs, the blade-tip clearance is gradually reduced to improve efficiency, which may lead to rubbing damage and affect safe operation. The mechanical properties of a bolted joint change significantly during the blade–casing rubbing process and influence the dynamic properties of the rotor system. Based on the finite element (FE) modeling method, a 15-node bolted joint rotor system model is established in this paper, in which the bolted joint is represented by a 2-node joint element, and the blade–casing rubbing force is considered. The Newmark method is used to solve the motion equations. The dynamic model is validated by comparing the frequency response characteristics for different numbers of blades with the results provided in other published studies. Based on the established model, the effects of the rotational speed, number of blades, and rubbing stiffness on the dynamic responses, normal rubbing forces, and bending stiffness of the bolted joint are evaluated by numerical simulation. The results show that the response amplitude and bending stiffness of the bolted joint change significantly under blade–casing rubbing faults, and the mean value of the vibration response deviates significantly from 0 as the number of blades increases. Meanwhile, the amplitude of the frequency component f_{VC} and the maximum value of the normal rubbing force also increase as the number of blades increases. The main contribution of this paper is the establishment of a new model for a bolted joint rotor system, considering the time-varying bending stiffness of the bolted joint and the blade–casing rub fault, comparing the simulation results to obtain some general results bridging the current research gap. Meanwhile, the numerical results in this paper can provide a cognitive basis for the blade–casing rubbing fault mechanism of a bolted joint rotor system under the influence of speed, number of blades, and rubbing stiffness. The nonlinear dynamic characteristics observed in the present paper can be applied to the blade–casing rubbing fault diagnosis of turbomachines.

Keywords: dynamic analysis; bolted joint; rotor system; blade–casing rubbing fault; bending stiffness

Citation: Wen, C.; Zhu, Z.; Fu, X.; Long, T.; Li, B. Dynamic Analysis of a Bolted Joint Rotor-Bearing System with a Blade–Casing Rubbing Fault. *Processes* **2023**, *11*, 2379. https://doi.org/10.3390/pr11082379

Received: 1 July 2023
Revised: 3 August 2023
Accepted: 4 August 2023
Published: 7 August 2023

1. Introduction

The bladed rotor is widely used in aeroengines (see Figure 1) for the transmission of power. In recent years, engineers have focused on reducing the blade–casing clearance to improve efficiency [1]. However, reducing the clearance increases the risk of blade–casing rubbing, leading to efficiency loss and affecting safe operation. Moreover, the mechanical properties of the bolted joint in an aeroengine rotor system change significantly during a blade–casing rubbing fault, which may further increase the vibration amplitude due to softening of the bolted joint bending stiffness [2]. This might result in complex

system vibration behavior and put security at risk. Hence, comprehensive research on the behavior of bolted joint rotor systems with blade–casing rubbing faults will help to control aeroengine safety risks.

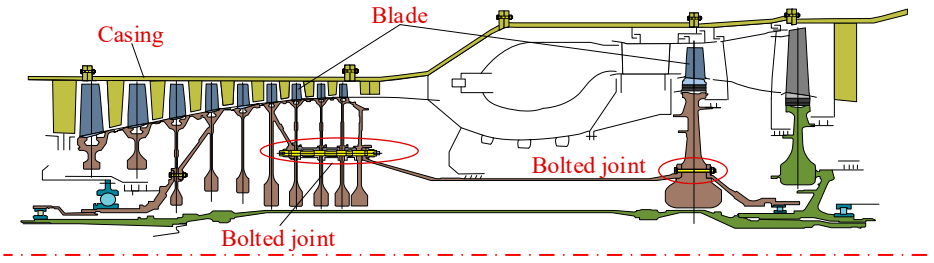

Figure 1. Illustration of the bolted joint rotor-casing system of an aeroengine compressor.

Many researchers have revealed the nonlinear effects of a blade-casing rub on rotor dynamics. Kou et al. [3] derived an improved dynamic model of a rotor system with wide-chord blades and pointed out that the swing motion may induce the edge failures of the blade. Jin et al. [4] established a finite element model of a dual-rotor-bearing system with coupling misalignment and blade–casing rubbing fault, and the component mode synthesis method was employed for order reduction of the established model. After comparing the numerical and experimental data, they came to the conclusion that when a blade–casing rubbing fault emerges, the casing vibration behavior is more sensitive than is the rotor. Yang et al. [5,6] analytically studied the nonlinear vibration features of a pedestal looseness rotor system undergoing a blade–casing rubbing fault. A blade-rotor-casing model was developed by Ma et al. [7]; they also examined the complex vibration characteristics brought on by a blade–casing rubbing defect. Using the finite element approach, Ma et al. [8] developed an excellent model of a shaft-disk-blade system and then discussed the impact of blade stagger angles, speeds, and casing stiffness on rubbing-induced dynamic phenomena. Zeng et al. [9] proposed an analytical model for blade–casing rubbing force, and the established model was verified using a dedicated test rig. Colaïtis et al. [10] presented a numerical simulation strategy based on the harmonic balance method to qualitatively characterize the blade dynamic features when blade casing contact occurs. Piollet et al. [11] established a 3D finite element model based on the open NASA rotor 37 compressor blade, and a benchmark for simulation and analyses was proposed. A parametric study on a misaligned rotor system with blade-stator contact was performed by Thiery et al. [12], and the dynamic properties of the coupling fault were revealed. A blade–casing rubbing fault in a Jeffcott rotor led Thiery et al. [13] to create a mathematical model of a bladed rotor to study the nonlinear dynamic behavior of the rotor. Through mathematical analysis and experimental investigation, Torkhani et al. [14] investigated the effects of the partial rubbing of a blade and stator on rotor dynamics. By accounting for the blade–casing rubbing problem, Wang et al. [15] proposed a dual-rotor-support-casing system model. They then carried out numerical and experimental research to examine the system's dynamic performance. In order to clearly describe the literature gap and the main current research contents regarding blade rubbing fault, the main research concerning the blade rubbing fault from the above literature is listed in Table 1. Based on a survey of the literature and Table 1, it can be noted that researchers are focused on the rub-impact between the integrated rotor-blade system and the casing. However, the rub-impact that occurs in the bolted joint rotor system has scarcely ever been investigated. According to the actual design of the aeroengine, a detailed investigation is required to comprehend how rub-impact affects the stiffness properties and rotor dynamics of the bolted joint rotor system.

Table 1. The main focus regarding the blade rubbing fault of the current investigation.

References	Type of Rubbing Fault	Research Contents	Typical Features
Kou et al. [3]	Local rub-impact fault between wide-chord blades and the casing.	Established an improved dynamic model of a rotor system with wide-chord blades, explore the impact of the gyroscopic effect and swing motion on rub-impact.	The swing motion may induce edge failures of the blade and aggravate the rub-impact fault, while the gyroscopic effect weakens the swing motion.
Jin et al. [4]	Local blade–casing rubbing fault of a dual-rotor-bearing system.	Established a finite element model of a dual-rotor-bearing system with coupling misalignment and blade–casing rubbing fault, exploring the nonlinear dynamics of the system at different rotational speed ratios.	There are complex frequency components in a dual-rotor-bearing system with blade–casing rubbing fault, including the fundamental frequency of the high and low-pressure shaft, the blade passing frequency, and their multiple frequency components.
Yang et al. [5,6]	Multiple local blade–casing rubbing faults of the rotor system.	Studied the nonlinear vibration features of a pedestal looseness rotor system undergoing a blade–casing rubbing fault.	The pedestal looseness would exacerbate the degree of rubbing fault and lead to the fault occurring in advance.
Ma et al. [7,8]	Local blade tip rubbing between the blade and casing.	Established a rubbing fault considering the effects of an elastic casing and examined the complex vibration characteristics with the change in speed brought on by a blade–casing rubbing defect.	The 2T-period motion introduced by the rubbing fault would be more apparent with increased speed and would appear to impact resonance.
Zeng et al. [9]	Local blade–casing rubbing.	Proposed an analytical model for blade–casing rubbing force, studied the dynamic behavior of the blade with different incursion depths, and verified the numerical result using a dedicated test rig.	A larger incursion depth would lead to an increase in the maximum value of the rubbing force, and the normal and tangential rubbing force conform to Coulomb's law of friction.
Piollet et al. [11]	Local blade–casing rubbing.	Established a 3D finite element model of a NASA rotor 37 compressor blade, investigated the system's response with different contact severity, and proposed a benchmark for simulation.	The lower contact severity would weaken the amplitude of the system.
Thiery et al. [12,13]	Local blade–casing rubbing fault considering the deform elastically of the blade.	Studied the nonlinear dynamic behavior of the bladed rotor by creating a mathematical model and performed a parametric study on a misaligned rotor system with blade-stator contact.	The nonlinear dynamics of system are similar to simple bladed Jeffcott rotors when scaled with the number of blades.
Torkhani et al. [14]	Light to heavy intermittent local blade–casing rubs.	Investigated the effects of the varying degrees partial rub of a blade and stator on rotor dynamics, both experimentally and numerically.	The increase in imbalance causes a heavier contact over a longer duration, and the contact effect would cause an abrupt increase in the rotor resonance frequency.
Wang et al. [15]	Local blade–casing rubbing fault considering the deformations of the blade and casing.	Proposed a dual-rotor-support-casing system model and investigated the effect of blade rubbing fault on the nonlinear dynamics of the system.	The blade passing frequency and its multiple frequency components allow for effectively distinguishing the blade–casing rubbing fault.

The bolted joint, which is one of the commonly employed structures used to join nearby components into integrated systems, can present enough stiffness to guarantee the integrity of the rotor system in an aeroengine [16–19]. However, several researchers via numerous in-depth surveys detected that the bolted joint structure exhibits intricate

mechanical properties. Zhou et al. [20] explored the effect of thread tooth profile, thread pitch, and the modulus ratio of bolt to nut on load distribution in threads using the ABAQUS codes, showing that the nut shape exerts significant effects on load distribution in the threads. Mir-Haidari et al. [21] suggested that the inconsistency between the numerical model and actual structure should be attributed to the higher nonlinear behavior of the bolted joint, proposing an analytical model which could accurately reflect the nonlinear dynamics of bolted joint. Zhou et al. [22] thoroughly investigated the effect of preload on the reliability of the bolted joint using finite element software; the result shows that there was a significant influence on the reliability of the bolted joint due to the change in preload. Therefore, the complex mechanical properties of the bolted joint increase the difficulty of analyzing the rotor dynamics under blade–casing rubbing faults. Du et al. [23] established the dynamic model of a tie-bolt rotor, based on the proposed virtual material method. Zhang et al. [24,25] analyzed the dynamic properties of a multi-disk rod fastening rotor system subjected to rub-impact failure and a cracked shaft. Zhao et al. [26] proposed a modeling method for the bolted joint structure in the rotor system considering the elastoplastic deformation at the mating interface, and the effectiveness of the model was verified by experimental results. Yu et al. [27] performed a simulation and experiment to reveal the effect of damping nonlinearity introduced by the spigot on a bolted joint rotor system. Li et al. [28,29] performed a numerical simulation to study the steady-stress distribution at the mating interface of a gas turbine tie-bolt rotor under different load conditions. Zhao et al. [30] and Wu et al. [31] proposed an assembly method of the contact stiffness matrix of the bolted joint and shaft elements for dynamic modeling of the rod-fastening rotor-bearing system. Zou et al. [32] analyzed the influence of the pretightening state at the mating surface of a bolted joint in a certain type of aeroengine rotor system on the rotor dynamic characteristics through finite element simulation and experimental study. Li et al. [33] found that the increase in bolt loosening degree and bolt in regards to looseness will lead to a decrease in natural frequencies and an increase in resonant response amplitudes through numerical and experimental study. Only the bolted joint modeling technique and the motion stability of the bolted joint rotor system—with or without a fixed-point rubbing fault—were taken into account in the above research. However, researchers have rarely explored the relationship between the blade–casing rubbing fault's influence law, the bolted joint's stiffness properties, and the vibration response. Because of the high speed and high load characteristics of the aeroengine rotor system, the instantaneous energy introduced by the blade–casing rub is considerable [3]. Therefore, the bolted joint bending stiffness characteristics and vibration response behavior of a bolted joint rotor system with multiple blades under a rubbing fault should be studied.

The major goal of this research is to identify the blade casing rub-impact dynamic properties of a rotor-bearing system with a bolted joint while taking into account the time-varying bending stiffness of the bolted joint. A blade–casing rubbing model of the bolted joint rotor system is created based on the finite element (FE) modeling approach and the bolted joint element presented in our earlier work [34]. In the current study, the Newmark approach is used to solve the nonlinear vibration responses of the rotor system and to demonstrate the changes in bending stiffness of the bolted joint under blade–casing rubbing faults. The remainder of the present work is organized as follows: the motion equations for the bolted joint rotor-bearing system with rubbing faults in the blade casing are derived in Section 2. In Section 3, the established model is verified by comparing the response spectra under the condition of different numbers of blades with the results in other studies. The result of the mathematical analysis of the rotor system at various rotational speeds, with different numbers of blades, and with various rubbing stiffnesses, are discussed in detail in Section 4. Finally, Section 5 summarizes the key conclusions. The novelty of the present work can be summarized as follows. This work presents: (1) a dynamic model of a bolted joint rotor system considering the time-varying bending stiffness of the bolted joint and the blade–casing rub fault; (2) the nonlinear dynamics of a bolted joint rotor system and the mechanical properties evolution process of the bolted joint, evaluated with the changes in

rotational speed; and (3) the effect of the number of blades and casing stiffness on rotor system nonlinear dynamics and the mechanical properties of the bolted joint.

2. Motion Equations for a Rotor System with Blade–Casing Rubbing Fault

Figure 2 is an FE model schematic of a bolted joint rotor-bearing system that considers the blade–casing rubbing fault. The number of blades and rotor–stator clearance are taken into account for establishing the blade–casing rubbing force model, in which the deformations of the blades are ignored. Neither the vibration nor the deformation of the casing are considered in the present paper. The bolted joint is simulated through the bolted joint element proposed in our previous work [34]. By combining the FE modeling method [35,36], the bolted joint rotor-bearing system will then be modeled dynamically. It should be mentioned that the bolted joint rotor-bearing system established in the present work is a mathematical model which fails to display the practical model structure; the overall bolted joint rotor system described in Figure 2 is simply the schematic diagram of the FE model.

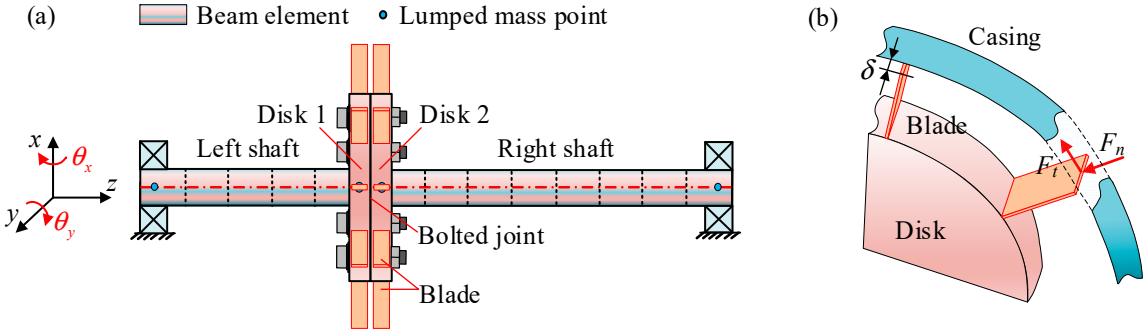

Figure 2. Bolted joint rotor-bearing system with blade–casing rubbing fault: (**a**) FE model of bolted joint rotor system; (**b**) sketch of blade–casing rubbing force.

2.1. Blade–Casing Rubbing Force Model

The blade–casing rubbing force acting at the *i*th blade is illustrated in Figure 3, where F_{ni} denot the normal force, F_{ti} defined the tangential force, ω_r is the rotating speed, and θ_{bi} represents the angle between the *i*th blade and the *y*-axis. The coordinate shown in Figure 3 is fixed at the location of the disk center when the rotor is not deformed, and then the angle θ_{bi} can be calculated by the following equation [37]:

$$\theta_{bi} = 2\pi i/N + \omega_r t \tag{1}$$

where i represents the *i*th blade, N is the number of uniformly distributed blades, and t represents the time instant.

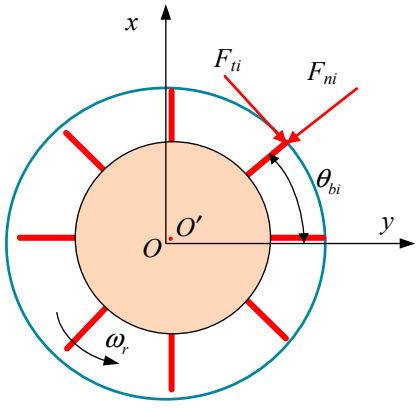

Figure 3. Schematic diagram of blade–casing rubbing procedure.

The blade is considered to be non-deformed during the rubbing procedure because the blade of the aeroengine rotor system is short and has relatively high stiffness. Therefore, the first mode of the blade is much higher than the maximum rotational and critical rotational frequency of the system, which indicates that the resonance behavior would not occur between the blades and the rotor system. By neglecting the bending deformation of the blade, the displacements at the ith blade tip in the x and y directions can then be calculated as follows:

$$\begin{cases} x_{bti} = x_d + (r_d + l_b)\cos(\theta_{bi}) \\ y_{bti} = y_d + (r_d + l_b)\sin(\theta_{bi}) \end{cases} \tag{2}$$

where x_d and y_d represent the vibration displacements of the disk at time instant t, r_d is the radius of the disk, and l_b is the length of the blade.

Let δ_i be the clearance between the ith blade and casing. The normal force introduced by the rubbing at the ith blade tip can be written as follows:

$$\begin{cases} F_{ni} = k_r \times (r_i - \delta_i), r_i \geq \delta_i \\ F_{ni} = 0, r_i < \delta_i \end{cases} \tag{3}$$

where k_r is the casing stiffness, r_i is the radial displacement at the ith blade tip, and $r_i = \sqrt{{x_{bti}}^2 + {y_{bti}}^2}$.

The tangential force at the ith blade tip can be expressed as follows:

$$F_{ti} = f \cdot F_{ni} \tag{4}$$

where f is the friction coefficient.

The rub forces at the ith blade tip in the x and y directions can then be calculated as

$$\begin{cases} F_{xi} = -F_{ni}\cos\theta_i + F_{ti}\sin\theta_{bi} \\ F_{yi} = -F_{ni}\sin\theta_i - F_{ti}\cos\theta_{bi} \end{cases} \tag{5}$$

When a rubbing fault develops, the sum of the rubbing force acting on N blades of rotor can be described using the sum of the force components operating in the x and y directions, as follows:

$$\begin{cases} F_x = \sum_{i=1}^{N} F_{xi} \\ F_y = \sum_{i=1}^{N} F_{yi} \end{cases} \tag{6}$$

2.2. Rolling Bearing Force Model

Two identical ball bearings maintain the rotor assembly in place. The Hertz contact theory may be used to calculate the bearing force, meeting the following hypotheses:

(a) The inner race is connected to the rotating shaft, and the outer race is connected to the bearing house so that no relative slippage occurs during operation of the rotor system.
(b) The rolling ball exhibits pure rolling, without a sliding motion, and the displacement between the balls is equal during operation.

Figure 4 shows a schematic diagram of the bearing, where N_b is the number of rolling balls and ω_c is the rotational speed of the cage, which can be calculated by

$$\omega_c = \omega_r \cdot r_i / (r_o + r_i) \tag{7}$$

where r_o denotes the radius of the bearing outer race, and r_i denotes the radius of the bearing inner race.

For the ball bearing, the compliance and stiffness will occur in periodic variation due to the periodic varying of the contact position between the races, which lead to a so-called varying compliance (VC) vibration. The VC vibration is an inherent characteristic and

always exists, even if under normal conditions. The VC vibration is in connection with the bearing structure parameter, and it can be given by:

$$\omega_{VC} = \omega_c \times N_b \tag{8}$$

The angle location of the ith rolling ball at time instant t can be expressed as

$$\theta_i = 2\pi(i-1)/N_\mathrm{b} + \omega_\mathrm{c} t \tag{9}$$

Based on the Hertz contact theory, the normal contact force between the ith rolling ball and raceway is obtained as [4–6]

$$f_{bi} = K_c(\delta_{bi})^{3/2} = K_c(x\cos\theta_i + y\sin\theta_i - \gamma_0)^{3/2} \cdot H(x\cos\theta_i + y\sin\theta_i - \gamma_0) \tag{10}$$

where K_c represent the Hertz contact stiffness; H (δ_{bi}) is the Heaviside function, where the contact deformation $\delta_{bi} = x\cos\theta_i + y\sin\theta_i - \gamma_0$; γ_0 is the bearing clearance

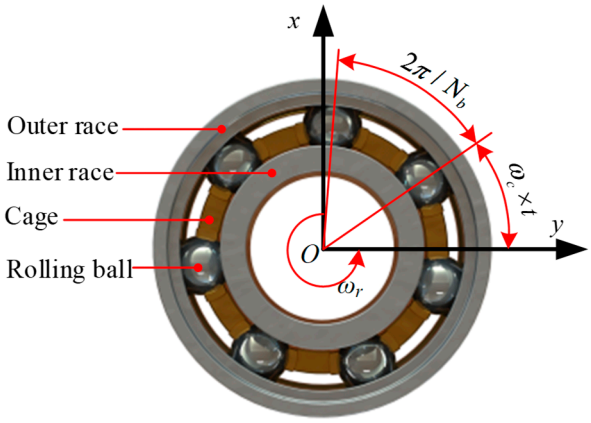

Figure 4. Schematic diagram of rolling bearing.

Finally, the bearing forces in the x and y directions generated by the rolling of the balls can be expressed as

$$\begin{cases} F_{bx} = \sum\limits_{i=1}^{N_b} f_{bix} = \sum\limits_{i=1}^{N_b} \left[K_c(x\cos\theta_i + y\sin\theta_i - \gamma_0)^{3/2} \cdot H(x\cos\theta_i + y\sin\theta_i - \gamma_0)\right]\cos\theta_i \\ F_{by} = \sum\limits_{i=1}^{N_b} f_{biy} = \sum\limits_{i=1}^{N_b} \left[K_c(x\cos\theta_i + y\sin\theta_i - \gamma_0)^{3/2} \cdot H(x\cos\theta_i + y\sin\theta_i - \gamma_0)\right]\sin\theta_i \end{cases} \tag{11}$$

2.3. Dynamic Model of Bolted Joint

The left and right shafts are connected by the bolted joint to produce an integrated rotor structure, as shown by the schematic diagram of a bolted joint rotor system in Figure 2. According to the global coordinate, the bending stiffness and lateral stiffness between the adjacent disks should be defined to connect the left and right shafts. Figure 5 shows the stiffness model between the adjacent disks of the bolted joint at the xz–plane, where the bending stiffness should be simulated by a piecewise linear stiffness model [2,38]. This is because tangential damping has almost no effect on the dynamic characteristics of the system [2]; only the macroscopic change of stiffness is considered, while failing to take into account the effect of the contact state of the mating interface on stiffness in the present work. In this paper, the lateral effect between the adjacent disks is simulated by a combination of a linear spring and a damping [see Figure 5b].

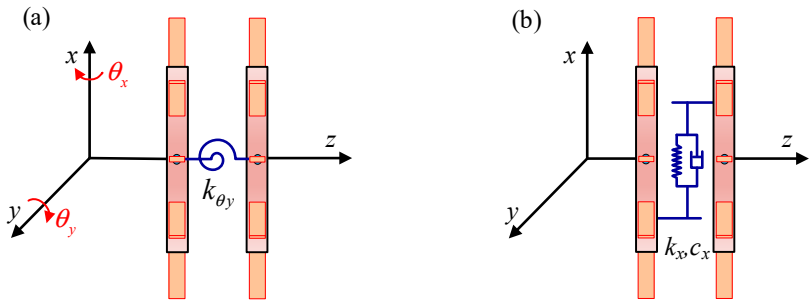

Figure 5. Stiffness between adjacent disks of a bolted joint in the *xz*–plane: (**a**) bending stiffness; (**b**) simple linear spring–damping model.

According to our previous work [34], the bolted joint can be modeled by the jointed element, which is based the Lagrange method, and whose mass, stiffness, and gyroscopic matrices are shown in Appendix A. Then, the governing equations of the bolted joint can be expressed as

$$\boldsymbol{M}_J^e \ddot{\boldsymbol{q}}_J^e + \left(\boldsymbol{C}_J^e - \omega_r \boldsymbol{G}_J^e\right)\dot{\boldsymbol{q}}_J^e + \boldsymbol{K}_J^e \boldsymbol{q}_J^e = \boldsymbol{Q}_J^e \tag{12}$$

where $\boldsymbol{M}_J^e$, $\boldsymbol{C}_J^e$, $\boldsymbol{G}_J^e$, and $\boldsymbol{K}_J^e$ are the mass, damping, gyroscopic, and stiffness matrices of the jointed element, which are shown in Appendix A; $\boldsymbol{q}_J^e$ represents the displacement vector of the bolted joint; and $\boldsymbol{Q}_J^e$ is the force matrix expressed by

$$\boldsymbol{Q}_J^e = \left[\begin{array}{cccccccc} m_1 e\omega_r{}^2\cos(\omega_r t) & m_2 e\omega_r{}^2\sin(\omega_r t) & 0 & 0 & m_1 e\omega_r{}^2\cos(\omega_r t) & m_2 e\omega_r{}^2\sin(\omega_r t) & 0 & 0 \end{array}\right]^{\mathrm{T}} \tag{13}$$

The proposed jointed element has eight degrees of freedom, and the displacement vector $\boldsymbol{q}_J^e$ can be written as:

$$\boldsymbol{q}_J^e = [u_1\ w_1\ \theta_1\ \varphi_1\ u_2\ w_2\ \theta_2\ \varphi_2]^{\mathrm{T}} \tag{14}$$

where u, w are the lateral displacements along the x and y axes, respectively; θ, φ are the rotational angles of the x- and y-axes, respectively; and subscripts 1 and 2 are associated with the two disks.

Additionally, the bolted joint's bending stiffness demonstrates piecewise linear properties, which can be written as [2]

$$k_\theta = \begin{cases} k_{\theta 1}, |\Phi| \leq |\Phi_0| \\ k_{\theta 2}, |\Phi| > |\Phi_0| \end{cases} \tag{15}$$

where k_θ denote the bending stiffness between the adjacent disks; $k_{\theta 1}$ and $k_{\theta 2}$ represent the bending stiffnesses at the first and second bending stages, respectively; Φ_0 is the relative rotation angle at the transition point; and Φ is the rotation angle between the adjacent disks, which can be calculated by Equation (15).

$$\Phi = \sqrt{(\theta_1 - \theta_2)^2 + (\varphi_1 - \varphi_2)^2} \tag{16}$$

The bending stiffness of the bolted joint should be determined using the following equation when the bending stiffness approaches the second bending stage [39]:

$$\widetilde{k}_{\theta 2} = k_{\theta 2} - \frac{\Phi_0}{\Phi}(k_{\theta 2} - k_{\theta 1}) \tag{17}$$

2.4. Global Motion Equations of Bolted Joint Rotor–Bearing System

The rotor shafts are modeled by the Timoshenko beam element, where the left shaft is dispersed into five shaft segments, and the right shaft is dispersed into eight shaft segments, as shown in Figure 2a. The bearing force acts on nodes at both ends of the rotor, and the

rigid disks of the bolted joint are located on the right node of the left shaft and on the left node of the right shaft [see Figure 2a]. The left and right shafts of the rotor system are connected through the bolted joint, which is simulated by the joint element described in Section 2.3. Based on the FE modeling method, the motion equations of the left and right shafts can then be written as

$$\boldsymbol{M}_L^s \ddot{\boldsymbol{q}}_L^s + (\boldsymbol{C}_L^s - \omega_r \boldsymbol{G}_L^s)\dot{\boldsymbol{q}}_L^s + \boldsymbol{K}_L^s \boldsymbol{q}_L^s = \boldsymbol{Q}_L^s \tag{18}$$

$$\boldsymbol{M}_R^s \ddot{\boldsymbol{\delta}}_R^s + (\boldsymbol{C}_R^s - \omega_r \boldsymbol{G}_R^s)\dot{\boldsymbol{\delta}}_R^s + \boldsymbol{K}_R^s \boldsymbol{\delta}_R^s = \boldsymbol{Q}_R^s \tag{19}$$

where $\boldsymbol{M}_L^s$ and $\boldsymbol{M}_R^s$ are the mass matrices of the left and right shafts; $\boldsymbol{C}_L^s$ and $\boldsymbol{C}_R^s$ are the damping matrices of the left and right shafts; $\boldsymbol{G}_L^s$ and $\boldsymbol{G}_R^s$ are the gyroscopic matrices of the left and right shafts; $\boldsymbol{K}_L^s$ and $\boldsymbol{K}_R^s$ represent the stiffness matrices of the left and right shafts, respectively; $\boldsymbol{q}_L^s$ and $\boldsymbol{q}_R^s$ are the displacement vectors corresponding to the left and right shafts; and $\boldsymbol{Q}_L^s$ and $\boldsymbol{Q}_R^s$ represent external force matrices. The mass, inertial, stiffness, and gyroscopic matrices of the beam element can be found in Appendix B. Although the FE modeling method can simulate the nearest state of the true structure, the excessive consideration of these factors would lead to a huge solve cost and even difficulty in convergence.

Based on the rotor dynamics and the motion equations of the bolted joint, left shaft, and right shaft presented in Equations (11), (16) and (17), the dynamic model of the bolted joint rotor system can be written as

$$\boldsymbol{M}\ddot{\boldsymbol{q}} + (\boldsymbol{C} - \omega_r \boldsymbol{G})\dot{\boldsymbol{q}} + \boldsymbol{K}\boldsymbol{q} = \boldsymbol{F}_g + \boldsymbol{F} \tag{20}$$

where $\boldsymbol{M}$ represents the mass matrix of the bolted joint rotor system, $\boldsymbol{C}$ represents the damping matrix of the bolted joint rotor system, $\boldsymbol{G}$ represents the gyroscopic matrix of the bolted joint rotor system, $\boldsymbol{K}$ represents the stiffness matrix of the bolted joint rotor system, $\boldsymbol{q}$ represents the displacement vector, F represents the external force vector of the overall rotor system, and F_g represents the gravity vector. The assembly methods of the mass, stiffness, and gyroscopic matrices of the beam elements and jointed element are shown in Figure 6.

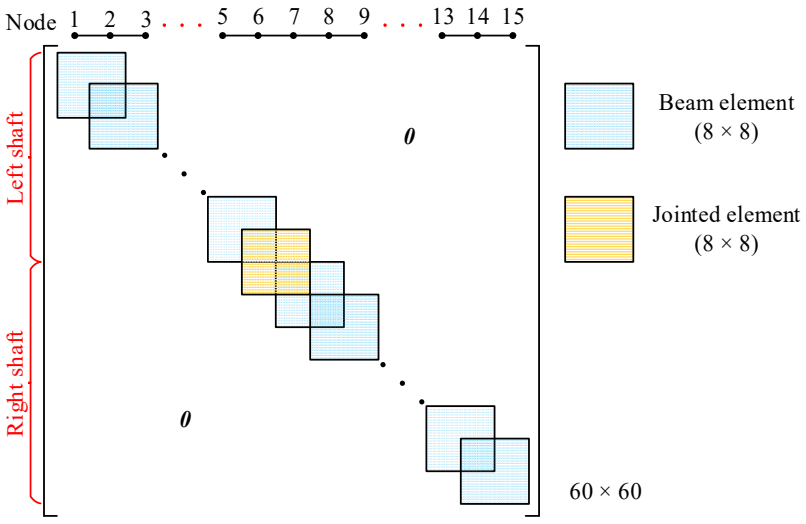

Figure 6. Assembly matrices of beam elements and jointed element.

Rayleigh damping is adopted to model the global damping matrix of the bolted joint rotor system in the present paper. This can be expressed as [40,41]

$$\boldsymbol{C} = a\boldsymbol{M} + b\boldsymbol{K} \tag{21}$$

The Rayleigh damping coefficients a and b can be calculated by Equation (22).

$$\begin{cases} a = 4\pi f_1 f_2(\xi_1 f_2 - \xi_2 f_1)/(f_2^2 - f_1^2) \\ b = (\xi_2 f_2 - \xi_1 f_1)/\pi(f_2^2 - f_1^2) \end{cases} \quad (22)$$

where f_1 and f_2 are the 1st and 2nd natural frequencies of the rotor system, and ξ_1 and ξ_2 are the modal damping ratios corresponding to f_1 and f_2, respectively.

To demonstrate the overall process of the modeling and solving in a more intuitive way, a detailed process of the numerical integration of the system, the calculation of the bending stiffness, and the assessment of rubbing fault are described in Figure 7.

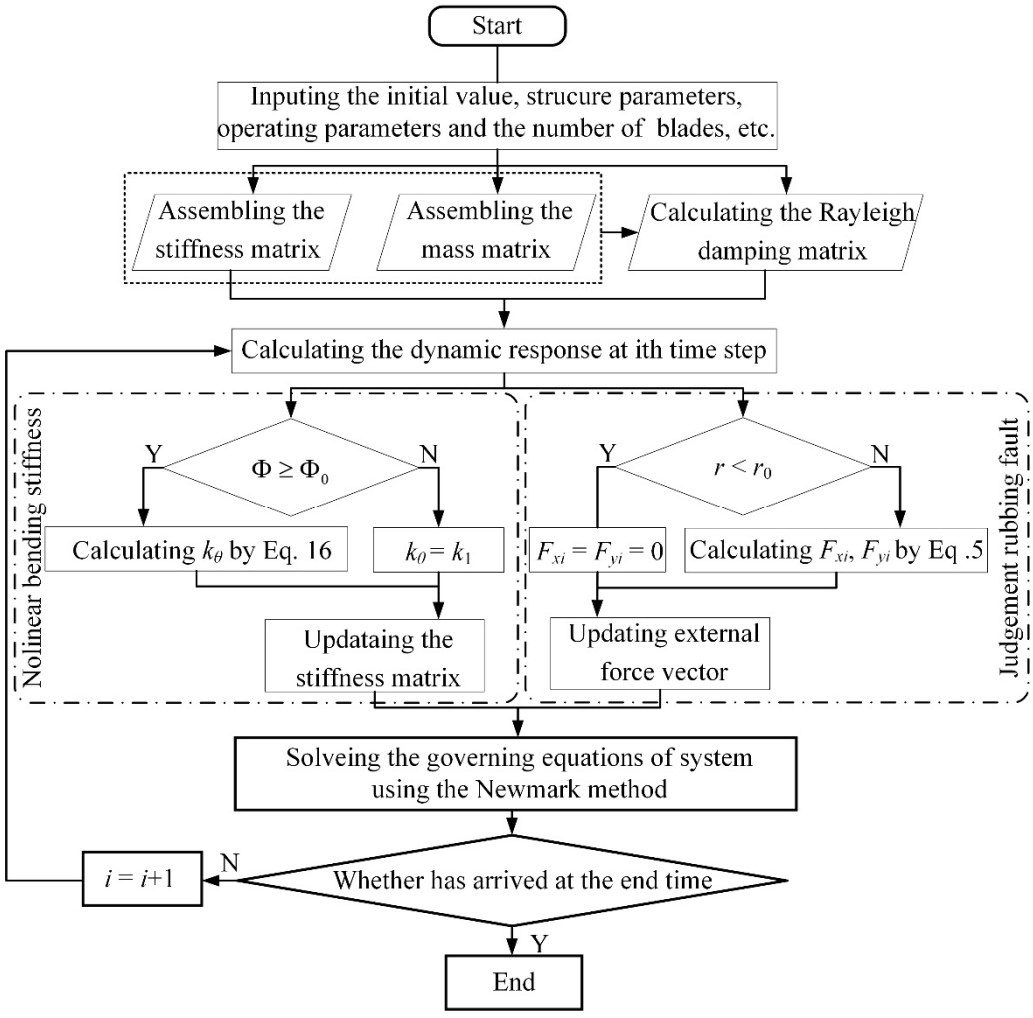

Figure 7. Flow diagram of the modeling and solving process for the system.

3. Verification Based on Response Spectra

The analytical and experimental data of a blade–casing rotor-bearing system from Ref. [4] are presented here to confirm the accuracy of the developed model. The detailed parameters of the rotor system and the experiment facility can be obtained from [4]. The outcome shows that when blade–casing rubbing problems occur, the rubbing frequency (equal to the product of the number of blades and the rotational frequency) is noticeable. The same numerical analysis conclusion can be found in [7,14,37]. Meanwhile, several researchers conducted corresponding blade–casing rubbing fault experiments using different types of rotor experiments and also captured the same behavior [4,6,15]. Therefore, in this section, the response spectra of the rotor system used in the present work, with blade–casing rubbing faults under different numbers of blades, are used to verify the established

model. The physical parameters of the bolted joint rotor system with blade–casing rubbing are presented in Table 2. Table 3 is a list of the ball bearings' structural parameters. The bolted-joint rotor system's waterfall diagrams can be obtained by applying the Newmark method. Then, a comparison among the working condition without blade–casing rubbing fault and the rubbing condition are presented for three different numbers of blades: N = 2, 4, and 6. The rotation speed is defined as ω_r = [6000:24,000] rev/min for the above working conditions, and the comparison results are shown in Figure 7.

Table 2. Physical parameters of bolted joint rotor system with blade–casing rubbing.

Physical Parameter	Value	Physical Parameter	Value
Length of the left shaft l_1 (m)	0.1	Friction coefficient f	0.1
Length of the right shaft l_2 (m)	0.16	Casing stiffness k_r (N/m)	5×10^6
Length of the blade l_b (m)	4.5×10^{-3}	Density of the shaft ρ (kg/m^3)	7850
Radius of the shaft r_s (m)	0.04	Poisson ratio of shaft element v	0.3
Diametral moment of inertia of disk 1 J_{d1} (kg·m^2)	7.5×10^{-3}	Eccentricity of disk 1 e_1 (m)	0.01×10^{-3}
Diametral moment of inertia of disk 2 J_{d2} (kg·m^2)	7.5×10^{-3}	Eccentricity of disk 2 e_2 (m)	0.01×10^{-3}
Polar moment of inertia of disk 1 J_{p1} (kg·m^2)	0.015	Mass of disk 1 m_1 (kg)	0.1
Polar moment of inertia of disk 2 J_{p2} (kg·m^2)	0.015	Mass of disk 2 m_2 (kg)	0.1
Elastic modulus of the shaft E (Gpa)	210	Radius of disk 1 r_{d1} (m)	7.3×10^{-3}
Initial blade–casing clearance δ (m)	0.1×10^{-3}	Radius of disk 2 r_{d2} (m)	7.3×10^{-3}

Table 3. Structural parameters of ball bearings.

Radius of Outer Race r_0 (mm)	Radius of Inner Race r_i (mm)	Numbers of Ball Elements N_b	Contact Stiffness K_c (N/m$^{3/2}$)	Bearing Clearance γ_0 (μm)
63.9	40.1	8	13.34×10^9	5

Figure 8a shows the waterfall diagram of the rotor system within ω_r = [6000:24,000] rev/min when the rubbing fault does not occur, in which the fundamental frequency f_r, varying compliance (VC) frequency f_{VC}, and their combination frequency components are the main frequency components. When the blade–casing rubbing force acts on the rotor system with 2 blades, the waterfall diagram corresponding to ω_r = [6000:24,000] rev/min, as shown in Figure 8b. Harmonic $2f_r$ emerges, and the combined frequency components f_{VC} and f_r appear in the three-dimensional spectrum simultaneously. This is because, under the blade–casing rubbing fault condition, the fault feature frequency manifests as the passing frequency of the blade, which is equal to $N{\cdot}f_r$, resulting in an increase in the amplitude corresponding to the harmonic $2f_r$. Similarly, as shown in Figure 8c,d, when N = 4 and 6, the passing frequency of the blade (equal to $N{\cdot}f_r$) appears in the waterfall diagrams with a rubbing fault. Therefore, the increased passing frequency of the blade can be seen as the typical characteristic of the blade–casing rubbing fault. Similarly, the same result could be observed in other researchers on the dynamic investigation of rotor systems with blade–casing rubbing faults. In Ref [4], researchers using a dual-rotor experimental rig to capture the blade–casing rubbing fault feature, which manifests as the increase in amplitude passing frequency of the blade. Yang et al. [6] noted the same behavior using the finite method and a dual-rotor-support-casing test rig: the increase in the amplitude of the harmonic N·f_r when the blade–casing rubbing fault occurred was analytically and experimentally investigated. Ma et al. [7] and Wang et al. [15] also captured the increase in the amplitude of the harmonic N·f_r using numerical simulation and experimentation. Hence, the correctness of the established model in the present paper could be proven from both numerical and experimental investigation, to a certain degree. It is worth noting that the low-frequency subharmonic motion introduced by the resonance of the ball bearing is not found in the system's waterfall diagrams. This is mainly attributed to the impact effect between the ball and the bearing ring being more obvious at a low rotation speed,

which would more likely generate a subharmonic vibration, while the bearing movement is relatively stable at a high rotation speed, and the response amplitude of the system is magnified, which will cause the subharmonic vibration to become imperceptible and even disappear. Particularly for the rotor system with the rubbing fault, the response amplitude of the system is significantly higher than the subharmonic vibration due to the extra excitation generated by the impact effect, which causes the subharmonic vibration to become ultimately become imperceptible.

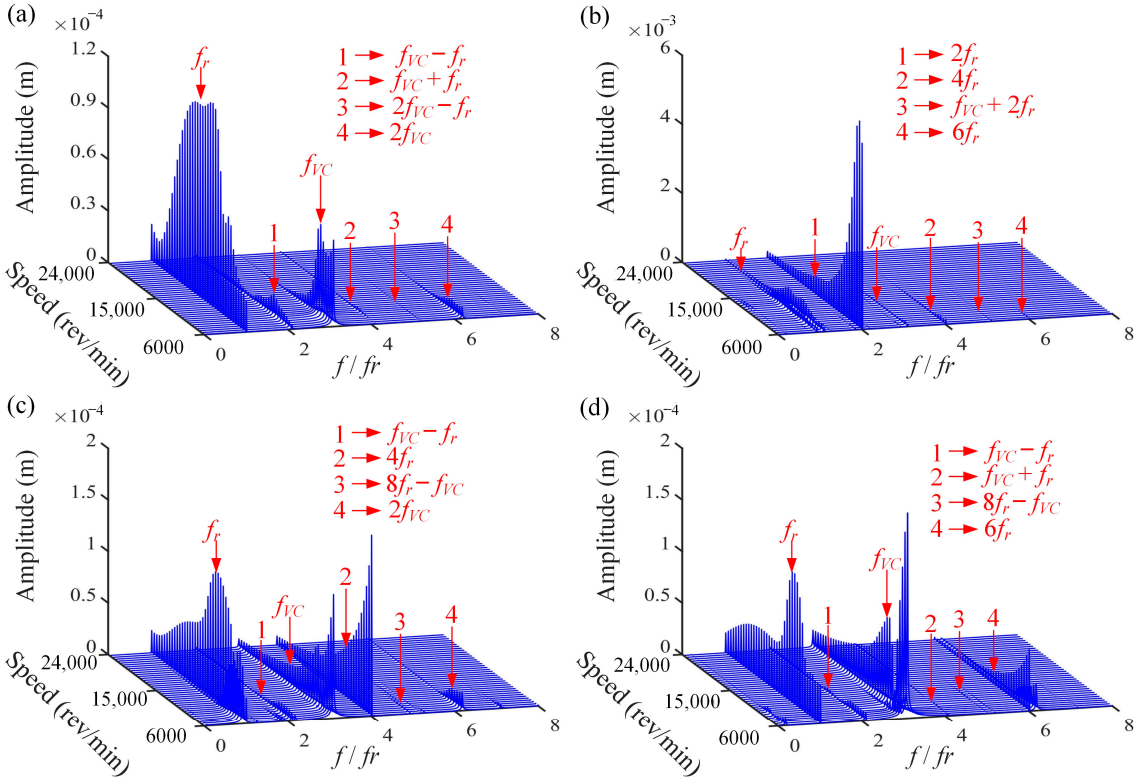

Figure 8. Waterfall diagrams of bolted joint rotor system with different numbers of blades: (**a**) without rubbing fault; (**b**) $N = 2$; (**c**) $N = 4$; (**d**) $N = 6$.

4. Numerical Simulation Results and Discussions

In this section, the Newmark method is used to solve the equations of motion. To avoid the transient solutions, we neglect the time-domain data of the first 150 cycles produced by numerical integration. Then, to study the blade–casing rubbing characteristics of the bolted joint rotor system, the waterfall diagrams, time-domain waveforms, spectra, normal rubbing force, and bending stiffness of the bolted joint are investigated deeply. The effects of the number of blades and the casing stiffness are discussed in detail in this section. The detailed structure dimensions and physical parameters of the bolted joint rotor-bearing system are listed in Tables 2 and 3.

4.1. Effects of Rotational Speed

In this section, we investigate the impact of the rotational speed ω_r on the dynamic response properties of the bolted joint rotor system under the blade–casing rubbing faults. The number of blades is defined as $N = 8$. By using the Newmark method, the spectrum cascades of disk 1, bending stiffness of the bolted joint, and amplitude-frequency curve are obtained, as shown in Figure 9, where the speed varies from 600 rev/min to 2400 rev/min in steps of 120 rev/min.

In Figure 9a, the fundamental frequency is denoted by f_r, and the VC frequency introduced by the ball bearing is denoted by f_{VC}. Frequency components such as f_r, f_{VC},

and the combined harmonics of f_r and f_{VC} appear in the waterfall diagram. In addition, the passing frequency of the blade, that is, $8{\cdot}f_r$, is excited due to blade–casing rubbing. The bending stiffness of the bolted joint structure during rotor operation, with time varying from 0.1 s to 0.13 s, is shown in Figure 9b. It can be seen that the bending stiffness changes continuously over time. This is because the bending stiffness enters the first and second stages as the relative angle between the adjacent disks constantly changes during operation, which can be explained by Equation (16). Moreover, the maximum value of bending stiffness decreases significantly with increasing rotational speed.

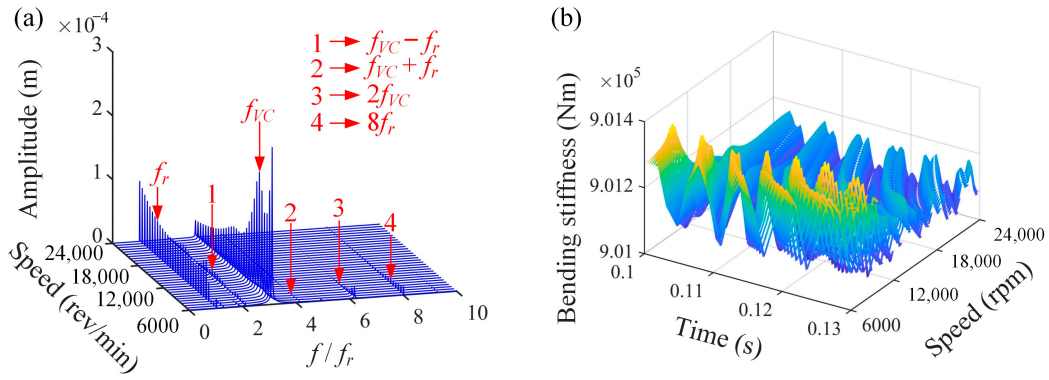

Figure 9. System response characteristics of the rotor system and bending stiffness of the bolted joint undergoing blade–casing rubbing fault: (**a**) waterfall diagram; (**b**) bending stiffness.

The time-domain waveform, frequency spectrum, normal rubbing force, and bending stiffness at ω_r = 6000, 12,000, and 18,000 rev/min, respectively, are displayed in Figure 10 to further investigate the impact of speed on the system's nonlinear dynamic. The fundamental frequency, VC frequency, its harmonics, and the passing frequency of the blade ($N{\cdot}f_r$) are illustrated in the frequency spectra. It should be mentioned that the amplitude corresponding to the fundamental frequency gradually increases with the change of speed and surpasses the amplitude of the VC frequency when the speed reaches a relatively high value of ω_r = 18,000 rev/min. Moreover, the passing frequency of the blade is always contained in the frequency spectra due to the rubbing fault occurring within the speed range. As observed from the diagrams of the normal rubbing force, a slight decrease in the maximum normal rubbing force can be found. According to Ref. [8], the normal rubbing force increases significantly as the rotational speed increases. The difference between the present work and Ref. [8] exists because the impact effect is weakened when the maximum amplitude of the system response decreases within the speed range of interest.

In Figure 11, the maximum and minimum values of the system responses and bending stiffnesses of the bolted joint at ω_r = 6000, 12,000, and 18,000 rev/min are demonstrated. In Figure 11a, the maximum and minimum amplitudes of the system responses at disk 1 are plotted, where the dynamic response amplitude of disk 1 decreases with an increase in rotational speed, as does the minimum value of the system response amplitude. Meanwhile, a decrease in the difference between the maximum value and minimum value of the system response can also be found as the speed increases, as shown in Figure 11a. This phenomenon occurs because the rubbing force decreases as the rotational speed increases, which is caused by a weakening of the impact effect due to a decrease in the maximum amplitude of the system response. For the bending stiffness of the bolted joint, Figure 11b demonstrates that the maximum bending stiffness decreases significantly when increasing the operating speed, but the minimum value of the bending stiffness changes slightly. To explain this phenomenon, the rotation angle between the adjacent disks at ω_r = 6000, 12,000, and 18,000 rev/min with time varying from 0.1 s to 0.13 s are obtained and shown in Figure 12. The obvious maximum value amplification phenomena of the rotation angle between the adjacent disks can be observed with increasing rotational speed, which leads

to the bending stiffness entering the second bending stage and a decrease in the maximum value of the bending stiffness.

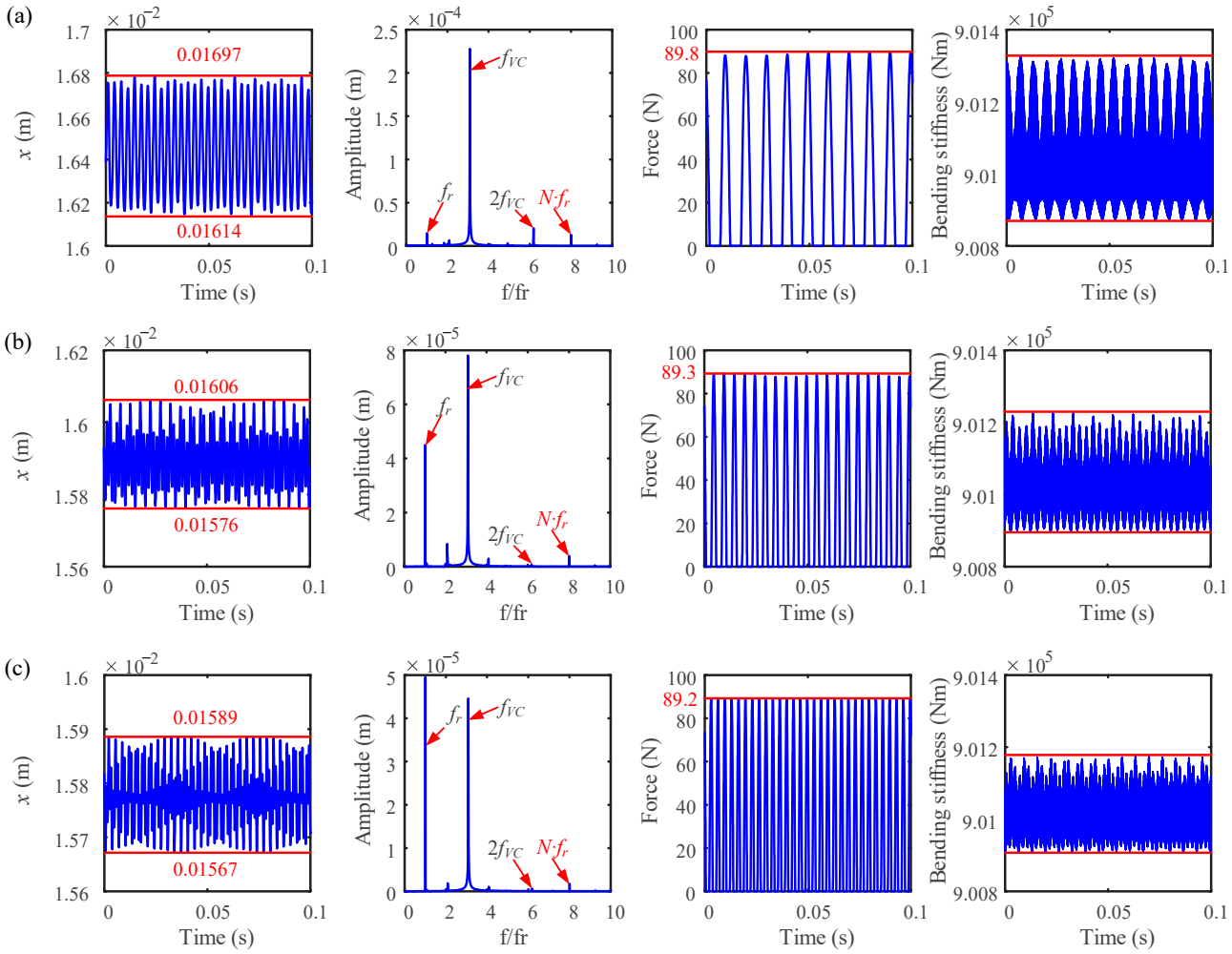

Figure 10. Vibration responses of a bolted joint rotor system with the blade–casing rubbing fault at different rotational speeds: (**a**) 6000 rev/min; (**b**) 12,000 rev/min; (**c**) 18,000 rev/min.

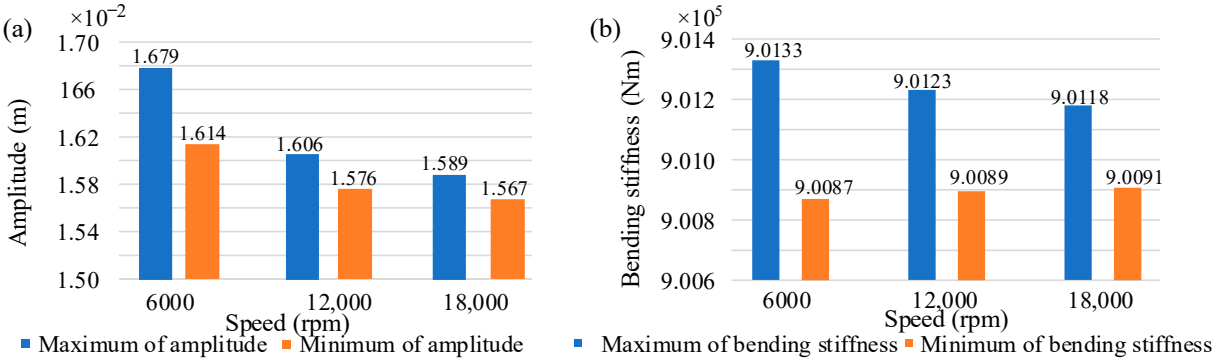

Figure 11. Maximum and minimum values of the system responses and bending stiffness of a bolted joint under different rotational speeds: (**a**) system response; (**b**) bending stiffness of bolted joint.

It should be mentioned that the relative angle between the adjacent disks of the bolted joint—where angle rotation along the *x*- and *y*-axes should be considered—is the rotation angle between the adjacent disks. In the present work, the rotation angle between the adjacent disks is calculated by Equation (15).

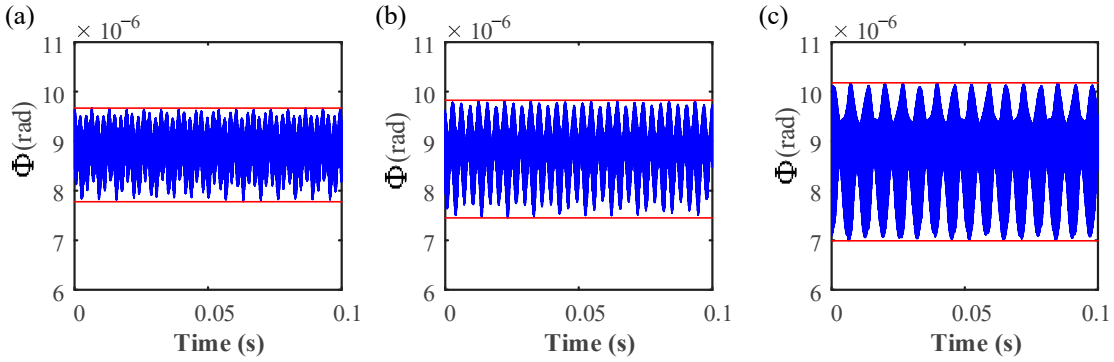

Figure 12. Rotation angle between the adjacent disks of a bolted joint during operation at: (**a**) 6000 rev/min; (**b**) 12,000 rev/min; and (**c**) 18,000 rev/min.

4.2. Effects of Number of Blades

The impact of the number of blades on the vibration characteristics of a rotor system with a bolted joint was the main focus of this parameter analysis. From Figure 8, it can be seen that the passing frequency of the blade appears in the spectra when blade–casing rubbing faults occur. The bending stiffness of the bolted joint within ω_r = [6000, 24,000] rev/min with the number of blades given as N = 0, 2, 4, and 6 are shown in Figure 13, with the aim of ascertaining the impact of the number of blades on the bending stiffness of the bolted joint This shows that the volatility of the bending stiffness is more intense due to a significant impact effect with 2 blades under the blade–casing rubbing fault, which makes the parameter value of the relative angle between disk 1 and disk 2 fluctuate over a wide range. This can also explain why the difference between the maximum and minimum values of bending stiffness under the condition of N = 2 are greater than those in other cases. Moreover, it can be seen that the bending stiffness decreases as the number of blades increases, and is even lower than the working condition without blade–casing rubbing faults when N = 8.

Time-domain waveforms and frequency spectra can help to reveal further information about rotor dynamic properties. To gain more insight into the dynamic performance of the bolted joint rotor system with blade–casing rubbing fault, the time-domain waveforms, frequency spectra, normal rubbing force, and bending stiffness at ω_r = 12,800 rev/min for different numbers of blades are obtained and are shown in Figure 14. Comparing the frequency component of the rotor system with and without the blade–casing rubbing fault, as seen in Figure 14, the most intuitive phenomenon is that the nonlinear feature of VC vibration and the passing frequency of a blade are highlighted in the presence of blade–casing rub-impact. That can be attributed to the fact that the impact effect between the ball and the race of the bearing is aggravated under the blade–casing rub-impact. The amplitude of the frequency component f_{VC} increases as N increases in the spectra, which can also indicate the aggravation of the bearing VC vibration. For the time-domain waveform of system, its complexity when a rubbing fault occurs and the response amplitude both change slightly as the number of blades increases. Moreover, the mean value of the system response is close to 0 for the working condition without a rubbing fault [see Figure 14a]. However, as the number of blades increases, the mean value of the vibration response deviates significantly from 0. This is also because the VC vibration under blade–casing rub-impact is more severe, and the impact force acting on disk 1 results in the mean value of the system responses deviating from the shaft axis. As for the normal rubbing force, the maximum value becomes greater due to the increase in the number of blades, described from 32.6 N to 37.7 N to 53 N. Moreover, the maximum and minimum values of the bending stiffness change significantly as the number of blades increases, which indicates that the number of blades has a significant effect on the bending stiffness of the bolted joint.

The maximum and minimum values of the system responses and bending stiffness of the bolted joint with various numbers of blades are presented in Figure 15 to further

demonstrate the impact of the number of blades on the system responses and bending stiffness of the bolted joint. The maximum value of the system response increases obviously when a rubbing fault occurs. The difference between the maximum and minimum values of the waveform with 2 blades is larger than that observed for the other numbers of blades [see Figure 15a]. This is because the impact effect is more obvious under the working condition of 2 blades subjected to a rubbing fault. As seen from Figure 15b, the amplitude of the normal rubbing force decreases as the number of blades increases. The primary cause is that as the vibration worsens over time due to a rubbing problem, and the rotation angle between the jointed disks rises, thus causing the bolted joint to approach its second stage of bending stiffness.

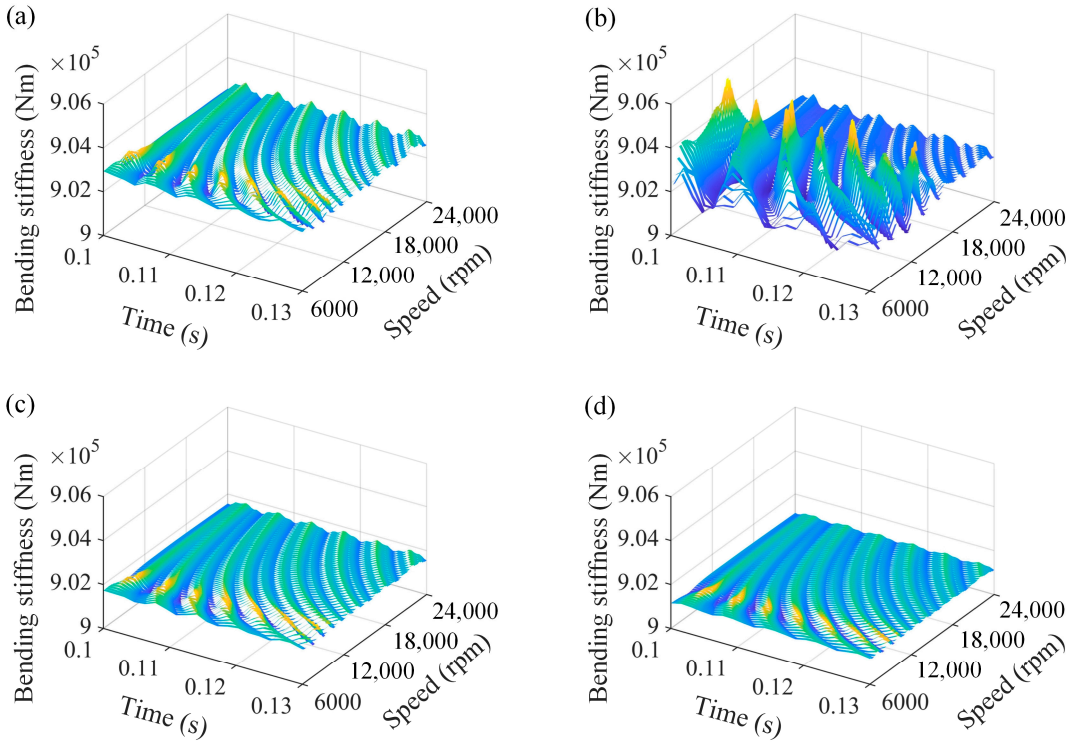

Figure 13. Bending stiffness of a bolted joint structure with a varying number of blades: (**a**) without rubbing fault; (**b**) N = 2; (**c**) N = 4; (**d**) N = 6.

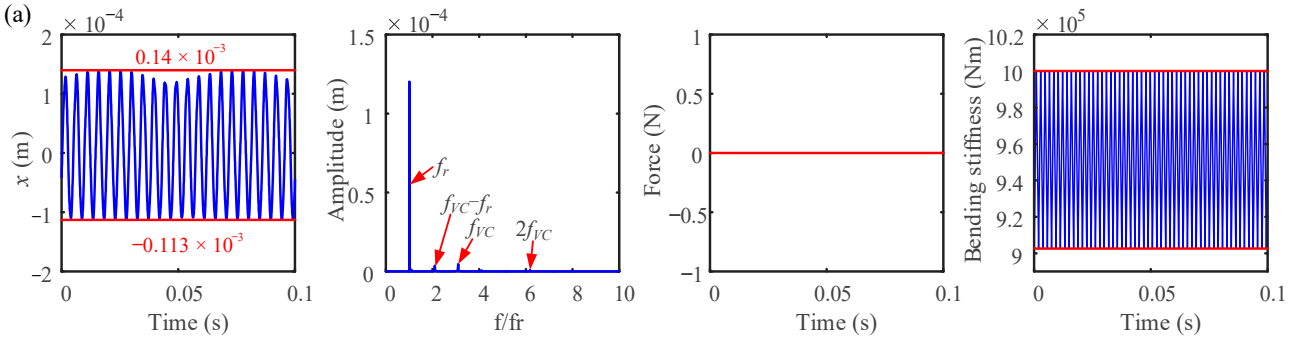

Figure 14. *Cont.*

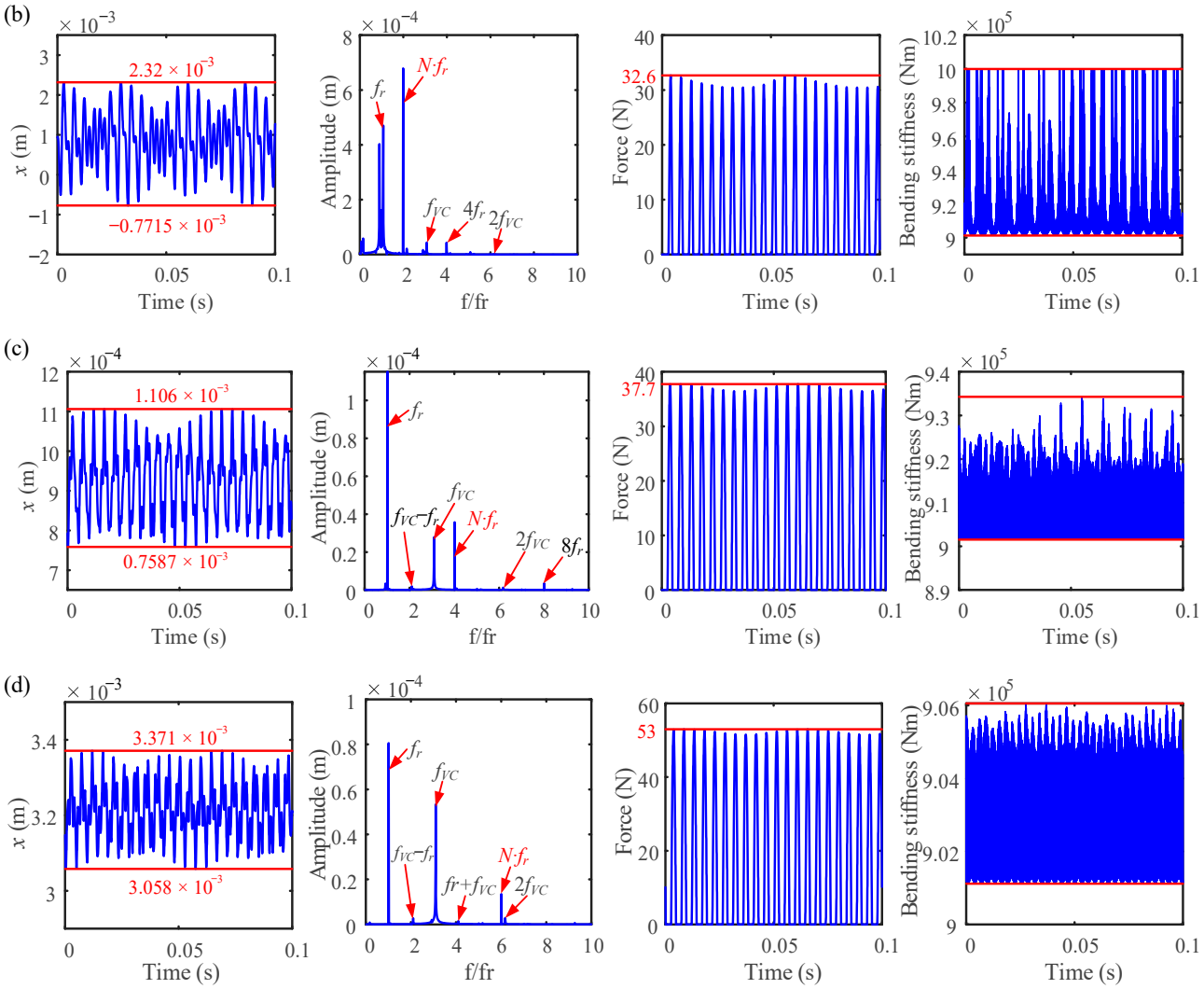

Figure 14. Vibration responses of a bolted joint rotor system at 12,800 rev/min: (**a**) without rubbing fault; (**b**) $N = 2$; (**c**) $N = 4$; (**d**) $N = 6$.

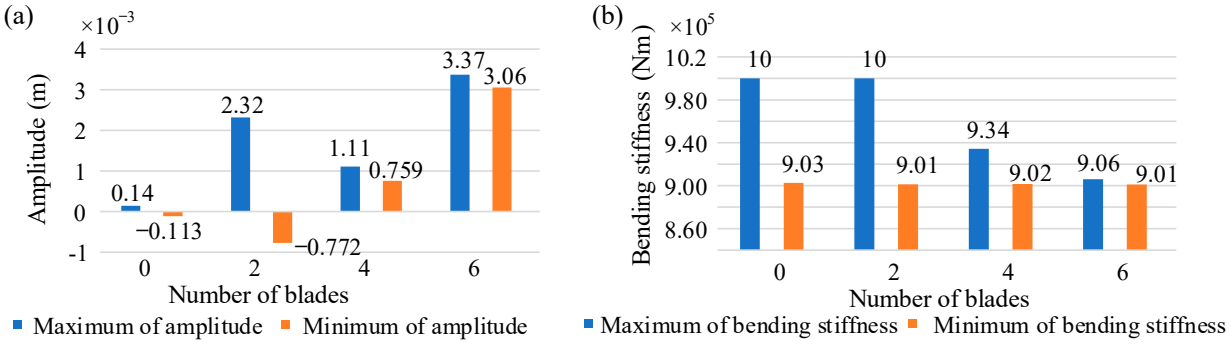

Figure 15. Maximum and minimum values of system responses and bending stiffness of a bolted joint with different numbers of blades: (**a**) system response; (**b**) bending stiffness of bolted joint.

4.3. Effects of Casing Stiffness

This section performs a frequency sweep analysis in advance to thoroughly understand the impacts of the casing stiffness on the blade–casing rubbing behavior of a bolted joint rotor system. The speed range is defined as ω_r = [6000, 24,000] rev/min, and the number of blades is set to $N = 4$. Figure 16 shows waterfall diagrams of the bolted joint rotor system

with casing stiffness k_r = 0 N/m, 1 × 10^6 N/m, 3 × 10^6 N/m, and 5 × 10^6 N/m. When the contact stiffness increases, the amplitude of the passing frequency of the blade ($N{\cdot}f_r$) increases significantly, while the frequency component remains consistent. This effect is explained by the fact that the frequency component $N{\cdot}f_r$ will become more evident, as the rubbing force increases simultaneously with the casing stiffness. In order to further explore the effect of casing stiffness on the nonlinear dynamics of the system, the time-domain waveforms, frequency spectra, normal rubbing force, and bending stiffness with casing stiffness k_r = 0 N/m, 1 × 10^6 N/m, 3 × 10^6 N/m, and 5 × 10^6 N/m are obtained by numerical simulation at a speed of 12,800 rev/min, as shown in Figure 17.

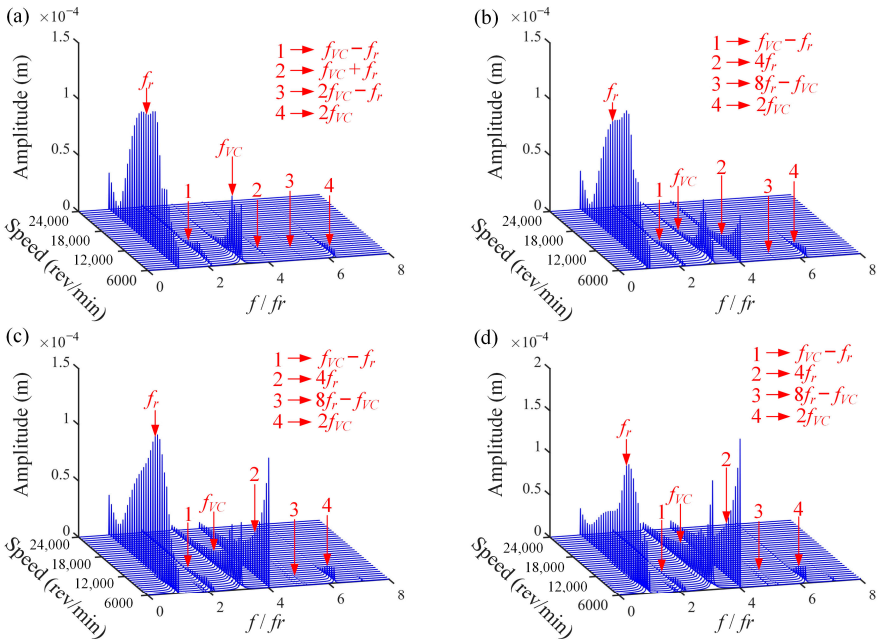

Figure 16. Waterfall diagrams of a bolted joint rotor system with different casing stiffnesses: (**a**) k_r = 0 N/m; (**b**) k_r = 1 × 10^6 N/m; (**c**) k_r = 3 × 10^6 N/m; (**d**) k_r = 5 × 10^6 N/m.

According to the Figure 17, the maximum value of the normal rubbing force increases with increasing casing stiffness, resulting in the mean value of the system response continuing to move away from 0, while the mean value of the system response is close to 0 when k_r = 0. In addition, with the increase in the casing stiffness, the maximum and minimum values of the system response continue to increase. That is because the larger casing stiffness would introduce a high rubbing force, which would lead to VC vibration becoming more severe and the impact force acting on disk 1 increasing, resulting in the mean value of the system responses deviating from the shaft axis. The amplitude of the VC frequency f_{VC}, the passing frequency of the blade $N{\cdot}f_r$, and the rubbing force increase in response to casing stiffness can also demonstrate this behavior. Moreover, the maximum bending stiffness decreased significantly when the casing stiffness increased to k_r = 5 × 10^6 N/m. This is due to the fact that when the lager rubbing force emerges on the bolted joint's disk, the relative angle of the joint increases, resulting in the bending stiffness reaching the second bending stage.

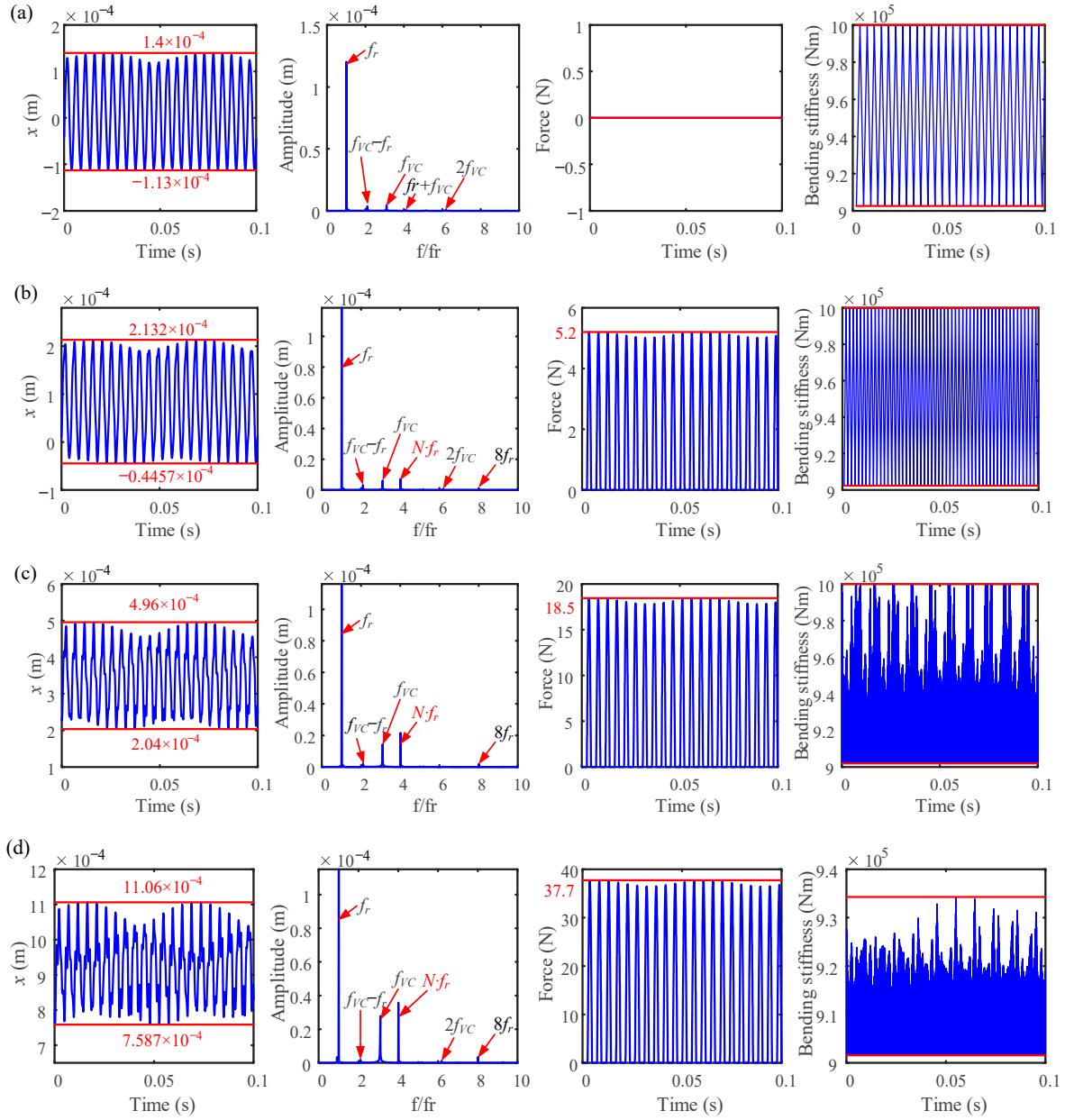

Figure 17. Vibration responses of bolted joint rotor system at 12,800 rev/min: (**a**) k_r = 0 N/m; (**b**) $k_r = 1 \times 10^6$ N/m; (**c**) $k_r = 3 \times 10^6$ N/m; (**d**) $k_r = 5 \times 10^6$ N/m.

5. Conclusions

In this work, a dynamic model of a bolted-joint rotor-bearing system was established in order to investigate the vibration properties of the rotor system and the bending stiffness of a bolted joint subjected to blade–casing rubbing faults. The model took into account the rubbing-impact between each blade and the case, as well as the bolted joint's piece-wise linear bending stiffness. Based on the developed model, quantitative research was performed to determine the effects of the rotational speed, the number of blades, and the casing stiffness on the system response and bending stiffness. The following are the primary conclusions obtained by numerical analysis:

1. When a rubbing fault occurs, the time-domain waveform becomes complicated, and the response amplitude changes slightly as the number of blades increases. As the number of blades increases, the mean value of the vibration response deviates significantly from 0.

2. The frequency component f_{VC}'s amplitude increases as the number of blades rises, and this increase in frequency also obviously raises the maximum value of the normal rubbing force. Furthermore, as the number of blades rises, the bending stiffness falls and eventually becomes even lower than it was under working conditions.
3. As the number of blades rises, the amplitude of the normal rubbing force decreases as the rotation angle between the adjacent disks increases; meanwhile, the bending stiffness of the bolted joint enters the second stage as a result of the vibration gradually being aggravated by the rubbing fault.
4. The rubbing effect becomes greater at a larger casing stiffness, and the amplitude of the passing frequency of the blade will increase significantly as the contact stiffness increases.

It should be emphasized that the main novelty of the present work is the proposed new dynamic model of a bolted-joint rotor-bearing system considering the time-varying bending stiffness of the bolted joint and the blade–casing rub fault. This includes an innovative analysis of the effects of the rotational speed, number of blades, and rubbing stiffness on the dynamic responses, normal rubbing forces, and bending stiffness of the bolted joint. However, this investigation is still focused on the local blade–casing rubbing fault of the rotor system. Indeed, there are numerous forms of blade–casing rubbing fault in the actual working condition of an aeroengine, such as intermittent rubbing faults, continuous full annular rubbing faults, etc. Therefore, the intermittent and continuous full annular rubbing faults will be further considered in our future work.

Author Contributions: C.W.: software and writing—original draft; Z.Z.: formal analysis and investigation; X.F.: supervision, writing—review, methodology, validation, and funding acquisition; T.L.: conceptualization, funding acquisition, and project administration; B.L.: data curation, writing—review and editing, and funding acquisition. All authors have read and agreed to the published version of the manuscript.

Funding: This research was supported by the Science and Technology Project of Guangxi, China, under Grant No. GK AD23026064; the Guangxi Natural Science Foundation, under Grant No. 2022GXNSFAA035550; the Middle-Aged and Young Teachers' Basic Ability Promotion Project of Guangxi, China, under Grant No. 2023KY0362; the National Natural Science Foundation of China, under Grant No. 52265006; and the Science and Technology Project of Guangxi, under Grant No. GK AD22080042.

Data Availability Statement: Data will be made available on reasonable request.

Conflicts of Interest: The authors declare no conflict of interest, including specific financial interest and relationships relevant to the subject of this paper.

Nomenclature

F_{ni}, F_{ti}	Normal and tangential force generated by the blade–casing rubbing (N)
N	Number of uniformly distributed blades
x_d, y_d	Vibration displacements of the disk (m)
r_d	Radius of the disk (m)
l_b	Length of the blade (m)
k_r	Casing stiffness ($N/m^{3/2}$)
r_i	Radial displacement at the ith blade tip (m)
F_x, F_y	Rubbing force acting on the rotor (N)
r_o, r_i	Outer and inner radius of the bearing (mm)
K_c	Hertz contact stiffness ($N/m^{3/2}$)
F_{bx}, F_{by}	Bearing forces in the x- and y-directions
$\boldsymbol{M}_J^e$, $\boldsymbol{C}_J^e$, $\boldsymbol{G}_J^e$, $\boldsymbol{K}_J^e$	Mass, damping, gyroscopic, and stiffness matrices of the jointed element
$\boldsymbol{q}_J^e$	Displacement vector of the bolted joint
$\boldsymbol{Q}_J^e$	Force matrix of the bolted joint

k_θ	Bending stiffness between the adjacent disks of the bolted-joint structure
$k_{\theta 1}$, $k_{\theta 2}$	Bending stiffnesses at the first and second bending stages
$\boldsymbol{M}_L^s$, $\boldsymbol{C}_L^s$, $\boldsymbol{G}_L^s$, $\boldsymbol{K}_L^s$	Mass, damping, gyroscopic, and stiffness matrices of the left shafts
$\boldsymbol{M}_R^s$, $\boldsymbol{C}_R^s$, $\boldsymbol{G}_R^s$, $\boldsymbol{K}_R^s$	Mass, damping, gyroscopic, and stiffness matrices of the right shafts
$\boldsymbol{q}_L^s$, $\boldsymbol{q}_R^s$	Displacement vector of the left shafts and right shafts
$\boldsymbol{Q}_L^s$, $\boldsymbol{Q}_R^s$	Force matrix of the left shafts and right shafts
M, C, G, K	Mass, damping, gyroscopic, and stiffness matrices of the rotor system
q	Displacement vector of the rotor system
F, F_g	Force matrix and gravity vector of the rotor system
f_1, f_2	The first and second natural frequencies
f_{bi}	Normal contact force between the ith rolling ball and the raceway
a, b	Rayleigh damping coefficients
N_b	Number of ball elements
N	Number of uniformly distributed blades
Greek letters	
ω_r	Rotating speed
θ_{bi}	Angle between the ith blade and the *y*-axis
δ_i	Clearance between the ith blade and casing
ω_c	Rotational speed of the cage
ω_{VC}	Frequency of varying compliance vibration
γ_0	Radial clearance of the bearing
δ_{bi}	Contact deformation of the bearing
γ_0	Radial clearance of the bearing
Φ	Rotation angle between the adjacent disks
Φ_0	Relative rotation angle at the transition point
ξ_1, ξ_2	Modal damping ratios

Appendix A

The mass, stiffness, and gyroscopic matrices of the jointed element are shown as follows:

$$\boldsymbol{M}_J^e = \begin{bmatrix} m_1 & & & & & & & \\ 0 & m_1 & & & & & & \\ 0 & 0 & J_{d1} & & & \text{sym} & & \\ 0 & 0 & 0 & J_{d1} & & & & \\ 0 & 0 & 0 & 0 & m_2 & & & \\ 0 & 0 & 0 & 0 & 0 & m_2 & & \\ 0 & 0 & 0 & 0 & 0 & 0 & J_{d2} & \\ 0 & 0 & 0 & 0 & 0 & 0 & 0 & J_{d2} \end{bmatrix} \tag{A1}$$

where m_i and J_{di} (i = 1, 2) represent the mass and diametral moment of inertia of the disks of the bolted joint, respectively.

$$\boldsymbol{K}_J^e = \begin{bmatrix} k_s & & & & & & & \\ 0 & k_s & & & & & & \\ 0 & 0 & k_\theta & & & \text{sym} & & \\ 0 & 0 & 0 & k_\theta & & & & \\ -k_s & 0 & 0 & 0 & k_s & & & \\ 0 & -k_s & 0 & 0 & 0 & k_s & & \\ 0 & 0 & -k_\theta & 0 & 0 & 0 & k_\theta & \\ 0 & 0 & 0 & -k_\theta & 0 & 0 & 0 & k_\theta \end{bmatrix} \tag{A2}$$

where k_θ and k_s represent the bending stiffness and lateral stiffness of the bolted joint, respectively.

$$\boldsymbol{C}_J^e = \begin{bmatrix} c_s & & & & & & & \\ 0 & c_s & & & & & & \\ 0 & 0 & c_\theta & & & \text{sym} & & \\ 0 & 0 & 0 & c_\theta & & & & \\ -c_s & 0 & 0 & 0 & c_s & & & \\ 0 & -c_s & 0 & 0 & 0 & c_s & & \\ 0 & 0 & -c_\theta & 0 & 0 & 0 & c_\theta & \\ 0 & 0 & 0 & -c_\theta & 0 & 0 & 0 & c_\theta \end{bmatrix} \tag{A3}$$

where c_θ and c_s represent the bending stiffness and lateral damping of the bolted joint, respectively.

$$\boldsymbol{G}_J^e = \begin{bmatrix} 0 & 0 & 0 & 0 & 0 & 0 & 0 & 0 \\ 0 & 0 & 0 & 0 & 0 & 0 & 0 & 0 \\ 0 & 0 & 0 & -J_{p1} & 0 & 0 & 0 & 0 \\ 0 & 0 & J_{p1} & 0 & 0 & 0 & 0 & 0 \\ 0 & 0 & 0 & 0 & 0 & 0 & 0 & 0 \\ 0 & 0 & 0 & 0 & 0 & 0 & 0 & 0 \\ 0 & 0 & 0 & 0 & 0 & 0 & 0 & -J_{p2} \\ 0 & 0 & 0 & 0 & 0 & 0 & J_{p2} & 0 \end{bmatrix} \tag{A4}$$

where J_{pi} (i = 1, 2) represent the polar moments of inertia of the disks of the bolted joint.

Appendix B

The mass matrix of the beam element can be written as

$$\boldsymbol{M}_T^e = \frac{\rho A l}{(1+\varphi_s)^2} \begin{bmatrix} M_{T1} & & & & & & & \\ 0 & M_{T1} & & & & & & \\ 0 & -M_{T4} & M_{T2} & & & symm & & \\ M_{T4} & 0 & 0 & M_{T2} & & & & \\ M_{T3} & 0 & 0 & M_{T5} & M_{T1} & & & \\ 0 & M_{T3} & -M_{T5} & 0 & 0 & M_{T1} & & \\ 0 & M_{T5} & M_{T6} & 0 & 0 & M_{T4} & M_{T2} & \\ -M_{T5} & 0 & 0 & M_{T6} & -M_{T4} & 0 & 0 & M_{T2} \end{bmatrix} \tag{A5}$$

where

$$\begin{aligned} &M_{\mathrm{T1}} = \tfrac{13}{35} + \tfrac{7}{10}\varphi_s + \tfrac{1}{3}\varphi_s^2,\ M_{\mathrm{T2}} = \left(\tfrac{1}{105} + \tfrac{1}{60}\varphi_s + \tfrac{1}{120}\varphi_s^2\right) l^2 \\ &M_{\mathrm{T3}} = \tfrac{9}{70} + \tfrac{3}{10}\varphi_s + \tfrac{1}{6}\varphi_s^2,\ M_{\mathrm{T4}} = \left(\tfrac{11}{210} + \tfrac{11}{120}\varphi_s + \tfrac{1}{24}\varphi_s^2\right) l \\ &M_{\mathrm{T5}} = \left(\tfrac{13}{420} + \tfrac{3}{40}\varphi_s + \tfrac{1}{24}\varphi_s^2\right) l,\ M_{\mathrm{T6}} = -\left(\tfrac{1}{140} + \tfrac{1}{60}\varphi_s + \tfrac{1}{120}\varphi_s^2\right) l^2 \\ &\varphi_s = \tfrac{12EI}{GA_s l^2},\ A_s = \tfrac{6A(1+\mu)}{7+6\mu},\ I = \tfrac{\pi}{64}\left(D^4 - d^4\right) \end{aligned} \tag{A6}$$

where D, d, and l denote the outer diameter, inner diameter, and length of the beam element; E, G, μ, and ρ represent the elastic modulus, shear modulus, Poisson ratio, and density of the beam element; A, I, A_s, and φ_s are the section area, second moment of area, effective shear area, and shear deformation coefficient of the cross-section of the beam element.

The inertial matrix of the beam element of the shaft can be expressed as

$$\boldsymbol{M}_R^e = \frac{\rho I}{l(1+\varphi_s)^2}\begin{bmatrix} M_{R1} & & & & & & & \\ 0 & M_{R1} & & & & & & \\ 0 & -M_{R4} & M_{R2} & & & symm & & \\ M_{R4} & 0 & 0 & M_{R2} & & & & \\ -M_{R1} & 0 & 0 & -M_{R4} & M_{R1} & & & \\ 0 & -M_{R1} & M_{R4} & 0 & 0 & M_{R1} & & \\ 0 & -M_{R4} & M_{R3} & 0 & 0 & M_{R4} & -M_{R2} & \\ M_{R4} & 0 & 0 & M_{R3} & -M_{R4} & 0 & 0 & M_{R2} \end{bmatrix} \tag{A7}$$

where

$$\begin{aligned} &M_{\mathrm{R1}} = \tfrac{5}{6},\ M_{\mathrm{R2}} = \left(\tfrac{2}{15} + \tfrac{1}{6}\varphi_s + \tfrac{1}{3}\varphi_s^2\right)l^2 \\ &M_{\mathrm{R3}} = -\left(\tfrac{1}{30} + \tfrac{1}{6}\varphi_s - \tfrac{1}{6}\varphi_s^2\right)l^2,\ M_{\mathrm{R4}} = \left(\tfrac{1}{10} - \tfrac{1}{2}\varphi_s\right)l \end{aligned} \tag{A8}$$

The stiffness matrix of the beam element of the bolt-joint rotor system can be calculated by

$$\boldsymbol{K}_B^e = \frac{EI}{l^3(1+\varphi_s)}\begin{bmatrix} K_{B1} & & & & & & & \\ 0 & K_{B1} & & & & & & \\ 0 & -K_{B4} & K_{B2} & & & symm & & \\ K_{B4} & 0 & 0 & K_{B2} & & & & \\ -K_{B1} & 0 & 0 & -K_{B4} & K_{B1} & & & \\ 0 & -K_{B1} & K_{B4} & 0 & 0 & K_{B1} & & \\ 0 & -K_{B4} & K_{B3} & 0 & 0 & K_{B4} & K_{B2} & \\ K_{B4} & 0 & 0 & K_{B3} & -K_{B4} & 0 & 0 & K_{B2} \end{bmatrix} \tag{A9}$$

where

$$K_{\mathrm{B1}} = 12,\ K_{\mathrm{B2}} = (4+\varphi_s)l^2,\ K_{\mathrm{B3}} = (2-\varphi_s)l^2,\ K_{\mathrm{B4}} = 6l \tag{A10}$$

The gyroscopic matrix of the beam element of the rotor system is expressed as

$$G^e = \frac{\rho I}{15l(1+\varphi_s)^2}\begin{bmatrix} 0 & & & & & & & \\ G_1 & 0 & & & & & & \\ -G_2 & 0 & 0 & & & antisymm & & \\ 0 & -G_2 & G_4 & 0 & & & & \\ 0 & G_1 & -G_2 & 0 & 0 & & & \\ -G_1 & 0 & 0 & -G_2 & G_1 & 0 & & \\ -G_2 & 0 & 0 & G_3 & G_2 & 0 & 0 & \\ 0 & -G_2 & -G_3 & 0 & 0 & G_2 & G_4 & 0 \end{bmatrix} \tag{A11}$$

where

$$G_1 = 36,\ G_2 = 3l - 15l\varphi_s,\ G_3 = l^2 + 5l^2\varphi_s - 5l^2\varphi_s^2,\ G_4 = 4l^2 + 5l^2\varphi_s + 10l^2\varphi_s^2 \tag{A12}$$

References

1. Ma, H.; Yin, F.; Guo, Y.; Tai, X.; Wen, B. A review on dynamic characteristics of blade-casing rubbing. *Nonlinear Dynam.* **2016**, *84*, 437–472. [CrossRef]
2. Qin, Z.Y.; Han, Q.K.; Chu, F.L. Analytical model of bolted disk-drum joints and its application to dynamic analysis of jointed rotor. *Proc. Inst. Mech. Eng. Part C J. Mech. Eng. Sci.* **2014**, *228*, 646–663. [CrossRef]
3. Kou, H.; Shi, Y.; Du, J.; Zhu, Z.; Zhang, F.; Liang, F.; Zeng, L. Rub-impact dynamic analysis of a rotor with multiple wide-chord blades under the gyroscopic effect and geometric nonlinearity. *Mech. Syst. Signal Process.* **2022**, *168*, 108563. [CrossRef]
4. Jin, Y.; Liu, Z.; Yang, Y.; Li, F.; Chen, Y. Nonlinear vibrations of a dual-rotor-bearing-coupling misalignment system with blade-casing rubbing. *J. Sound Vib.* **2021**, *497*, 115948. [CrossRef]
5. Yang, Y.; Chen, G.; Ouyang, H.; Yang, Y.; Cao, D. Nonlinear vibration mitigation of a rotor-casing system subjected to imbalance-looseness-rub coupled fault. *Int. J. Nonlin. Mech.* **2020**, *122*, 103467. [CrossRef]

6. Yang, Y.; Ouyang, H.; Yang, Y.; Cao, D.; Wang, K. Vibration analysis of a dual-rotor-bearing-double casing system with pedestal looseness and multi-stage turbine blade-casing rub. *Mech. Syst. Signal Process.* **2020**, *143*, 106845. [CrossRef]
7. Ma, H.; Yin, F.; Wu, Z.; Tai, X.; Wen, B. Nonlinear vibration response analysis of a rotor-blade system with blade-tip rubbing. *Nonlinear Dynam.* **2016**, *84*, 1225–1258. [CrossRef]
8. Ma, H.; Lu, Y.; Wu, Z.; Tai, X.; Wen, B. Vibration response analysis of a rotational shaft-disk-blade system with blade-tip rubbing. *Int. J. Mech. Sci.* **2016**, *107*, 110–125. [CrossRef]
9. Zeng, Z.; Zhang, D.; Tong, R.; Xu, H. Experimental investigation and analytical modeling for blade-casing rubbing force. *Mech. Syst. Signal Process.* **2022**, *167*, 108548. [CrossRef]
10. Colaïtis, Y.; Batailly, A. The harmonic balance method with arc-length continuation in blade-tip/casing contact problems. *J. Sound Vib.* **2021**, *502*, 116070. [CrossRef]
11. Piollet, E.; Nyssen, F.; Batailly, A. Blade/casing rubbing interactions in aircraft engines: Numerical benchmark and design guidelines based on nasa rotor 37. *J. Sound Vib.* **2019**, *460*, 114878. [CrossRef]
12. Thiery, F.; Gustavsson, R.; Aidanpää, J.O. Dynamics of a misaligned kaplan turbine with blade-to-stator contacts. *Int. J. Mech. Sci.* **2015**, *99*, 251–261. [CrossRef]
13. Thiery, F.; Aidanpää, J. Nonlinear vibrations of a misaligned bladed jeffcott rotor. *Nonlinear Dynam.* **2016**, *86*, 1807–1821. [CrossRef]
14. Torkhani, M.; May, L.; Voinis, P. Light, medium and heavy partial rubs during speed transients of rotating machines: Numerical simulation and experimental observation. *Mech. Syst. Signal Process.* **2012**, *29*, 45–66. [CrossRef]
15. Wang, N.; Liu, C.; Jiang, D. Experimental analysis of dual-rotor-support-casing system with blade-casing rubbing. *Eng. Fail. Anal.* **2021**, *123*, 105306. [CrossRef]
16. Qin, Z.Y.; Han, Q.K.; Chu, F.L. Bolt loosening at rotating joint interface and its influence on rotor dynamics. *Eng. Fail. Anal.* **2016**, *59*, 456–466. [CrossRef]
17. Zhao, S.; Zhang, L.; Zhu, R.; Han, Q.; Qin, Z.; Chu, F. Modeling approach for flexible shaft-disk-drum rotor systems with elastic connections and supports. *Appl. Math. Model.* **2022**, *106*, 402–425. [CrossRef]
18. Zhang, Y.; Xiang, L.; Su, H.; Hu, A.; Yang, X. Dynamic analysis of composite rod fastening rotor system considering multiple parameter influence. *Appl. Math. Model.* **2022**, *105*, 615–630. [CrossRef]
19. Li, T.; Yang, D.; Zhao, B.; Sun, Q.; Huo, J.; Sun, W. Measured and investigated nonlinear dynamics parameters on bolted flange joints of combined rotor. *J. Mech. Sci. Technol.* **2021**, *35*, 1841–1850. [CrossRef]
20. Zhou, W.; Zhang, R.; Ai, S.; He, R.; Pei, Y.; Fang, D. Load distribution in threads of porous metal–ceramic functionally graded composite joints subjected to thermomechanical loading. *Compos. Struct.* **2015**, *134*, 680–688. [CrossRef]
21. Mir-Haidari, S.; Behdinan, K. Nonlinear effects of bolted flange connections in aeroengine casing assemblies. *Mech. Syst. Signal Process.* **2022**, *166*, 108433. [CrossRef]
22. Zhou, W.; Ai, S.; Chen, M.; Zhang, R.; He, R.; Pei, Y.; Fang, D. Preparation and thermodynamic analysis of the porous zro2/(zro2 + ni) functionally graded bolted joint. *Compos. Part B Eng.* **2015**, *82*, 13–22. [CrossRef]
23. Du, B.; Qin, Z.; Lu, Q.; Wang, B.; Li, C. Dynamic modeling of tie-bolt rotors via fractal contact theory and virtual material method. *Proc. Inst. Mech. Eng. Part C J. Mech. Eng. Sci.* **2022**, *236*, 2141141063. [CrossRef]
24. Zhang, Y.; Liu, S.; Xiang, L.; Hu, A. Dynamic analysis of a multi-disk rod fastening rotor system with rub-impact based on multiple parameters. *Nonlinear Dynam.* **2022**, *107*, 2133–2152. [CrossRef]
25. Zhang, Y.; Xiang, L.; Hu, A.; Chen, K. Nonlinear dynamic response on multi-fault rod fastening rotor with variable parameters. *Appl. Math. Model.* **2023**, *114*, 147–161. [CrossRef]
26. Zhao, R.; Jiao, Y.; Chen, Z.; Li, Z.; Qu, X. Nonlinear analysis of a dual-disk rotor system considering elastoplastic contact. *Int. J. Nonlin. Mech.* **2022**, *141*, 103925. [CrossRef]
27. Yu, P.; Li, L.; Chen, G.; Yang, M. Dynamic modelling and vibration characteristics analysis for the bolted joint with spigot in the rotor system. *Appl. Math. Model.* **2021**, *94*, 306–331. [CrossRef]
28. Li, P.; Yuan, Q. Stress variation of a gas turbine tie-bolt rotor with hirth serrations considering assembling and thermal effects. *Proc. Inst. Mech. Eng. Part C J. Mech. Eng. Sci.* **2020**, *234*, 4932–4944. [CrossRef]
29. Li, P.; Yuan, Q. Determination of contact stiffness and damping of a tie-bolt rotor with interference fits using model updating with thin-layer elements. *Shock Vib.* **2020**, *2020*, 1–10. [CrossRef]
30. Wang, L.; Wang, A.; Jin, M.; Yin, Y.; Heng, X.; Ma, P. Nonlinear dynamic response and stability of a rod fastening rotor with internal damping effect. *Arch. Appl. Mech.* **2021**, *91*, 3851–3867. [CrossRef]
31. Wu, X.; Jiao, Y.; Chen, Z.; Ma, W. Establishment of a contact stiffness matrix and its effect on the dynamic behavior of rod-fastening rotor bearing system. *Arch. Appl. Mech.* **2021**, *91*, 3247–3271. [CrossRef]
32. Zou, C.; Xia, H.; Chen, K.; Zhai, J.; Han, Q. Research on the identification method of the pre-tightening state of the matching surface of the aero-engine disk-drum rotor. *Eng. Fail. Anal.* **2022**, *136*, 106208. [CrossRef]
33. Li, H.; Lv, H.; Sun, H.; Qin, Z.; Xiong, J.; Han, Q.; Liu, J.; Wang, X. Nonlinear vibrations of fiber-reinforced composite cylindrical shells with bolt loosening boundary conditions. *J. Sound Vib.* **2021**, *496*, 115935. [CrossRef]
34. Li, Y.; Luo, Z.; Liu, J.; Ma, H.; Yang, D. Dynamic modeling and stability analysis of a rotor-bearing system with bolted-disk joint. *Mech. Syst. Signal Process.* **2021**, *158*, 107778. [CrossRef]
35. Li, L.; Luo, Z.; He, F.; Ding, Z.; Sun, K. A partial similitude method for vibration responses of rotor systems: Numerical and experimental verification. *Int. J. Mech. Sci.* **2021**, *208*, 106696. [CrossRef]

36. Li, L.; Luo, Z.; He, F.; Sun, K.; Yan, X. An improved partial similitude method for dynamic characteristic of rotor systems based on levenberg-marquardt method. *Mech. Syst. Signal Process.* **2022**, *165*, 108405. [CrossRef]
37. Chen, G. Simulation of casing vibration resulting from blade-casing rubbing and its verifications. *J. Sound Vib.* **2016**, *361*, 190–209. [CrossRef]
38. Shuguo, L.; Yanhong, M.; Dayi, Z.; Jie, H. Studies on dynamic characteristics of the joint in the aero-engine rotor system. *Mech. Syst. Signal Process.* **2012**, *29*, 120–136. [CrossRef]
39. Yang, T.; Ma, H.; Qin, Z.; Guan, H.; Xiong, Q. Coupling vibration characteristics of the shaft-disk-drum rotor system with bolted joints. *Mech. Syst. Signal Process.* **2022**, *169*, 108747. [CrossRef]
40. Zhao, R.; Jiao, Y.; Qu, X. Scaling design strategy for experimental rotor systems subjected to restricted support stiffness. *Appl. Math. Model.* **2022**, *109*, 265–282. [CrossRef]
41. Pan, W.; Ling, L.; Qu, H.; Wang, M. Coupling dynamic behavior of aero-engine rotor system caused by rolling, pitching and yawing maneuver loads. *Appl. Math. Model.* **2022**, *102*, 726–747. [CrossRef]